Chinese Chemical Society | Xiamen University

Journal of Electrochemistry

Online First

11-21-2023

Nickel-Catalyzed α-Arylation of α-Cyanoacetates Enabled by Electrochemistry

Zi-Meng Li

Zhang-Jian Li

Anat Milo

Ping Fang

Tian-Sheng Mei

RESEARCH ARTICLE

DOI: 10.61558/2993-074X.3435 **Article ID:** 1006-3471(2023)00-0000-00

Http://electrochem.xmu.edu.cn

Nickel-Catalyzed α-Arylation of α-Cyanoacetates Enabled by Electrochemistry

Zi-Meng Li [a], Zhang-Jian Li [a,b], Anat Milo [c], Ping Fang [a,*], and Tian-Sheng Mei [a,*]

Dedicated to Professor Li-Xin Dai on the occasion of his 100th birthday

a Z.-M. Li, Z.-J. Li, Prof. Dr. P. Fang, and Prof. Dr. T.-S. Mei
State Key Laboratory of Organometallic Chemistry,
Shanghai Institute of Organic Chemistry, University of Chinese Academy of Sciences, Chinese Academy of Sciences
Shanghai 200032, China
E-mail: pfang@sioc.ac.cn, mei7900@sioc.ac.cn

b Z.-J. Li
College of Chemistry and Materials Science
Sichuan Normal University
Chengdu 610068, China

c Prof. Dr. A. Milo
Department of Chemistry
Ben-Gurion University of the Negev
Beer-Sheva 841051, Israel

Supporting information for this article is given via a link at the end of the document.

Keywords: organic electrosynthesis • nickel-catalysis • paired electrolysis • α-arylation • DFT calculation

Abstract: β-Amino acids have a wide range of applications in the field of pharmaceuticals. Utilizing a combination strategy of nickel catalysis and paired electrolysis, a catalytic α-arylation protocol of carbonyl compounds has been developed. This protocol affords various α-aryl-α-cyanoacetates, which can be reduced to high-value-added α-aryl-β-amino acids. The cross-coupling reaction of electron-deficient aryl bromides with α-cyanoacetates yields the expected products with good yields and functional group compatibility under mild conditions. Excessive electron-richness in initial aryl bromides facilitates the self-coupling of desired products. DFT calculations confirm that the presence of electron-rich aryl substitutions decreases the reduction potentials of the product anions, making them more susceptible to oxidation at the anode. Based on electroanalyses and mechanistic studies, it is proposed that the enolate intermediate, rather than the radical intermediate, participates in the catalytic cycle.

Introduction

In recent years, the β-amino acid scaffold has been applied to various drug molecules, mostly β-peptides (oligomers of β-amino acids) (**Figure 1**). Due to their unique structures, β-peptides exhibit distinctive properties: (1) β-peptides have predictable folding behaviors; (2) the behaviors of β-peptides are similar to those of α-peptides in peptide–protein and protein–protein interactions; and (3) β-peptides exhibit metabolic stability and can resist hydrolyses of peptidases[1]. β^3-amino acids (β-amino acids with 3-site side chains) can be conveniently synthesized from their corresponding α-amino acids via Arndt–Eistert reaction[2], thus almost all the β^3-amino acids with proteinogenic side chains are commercially available[1]. However, the synthesis of β^2-amino acids (β-amino acids with 2-site side chains), especially when side chains are aryl groups, is more challenging. In this situation, the α-arylation strategy is frequently implemented to flexibly adjust kinds of aryl groups, requiring the employment of palladium, copper, etc.

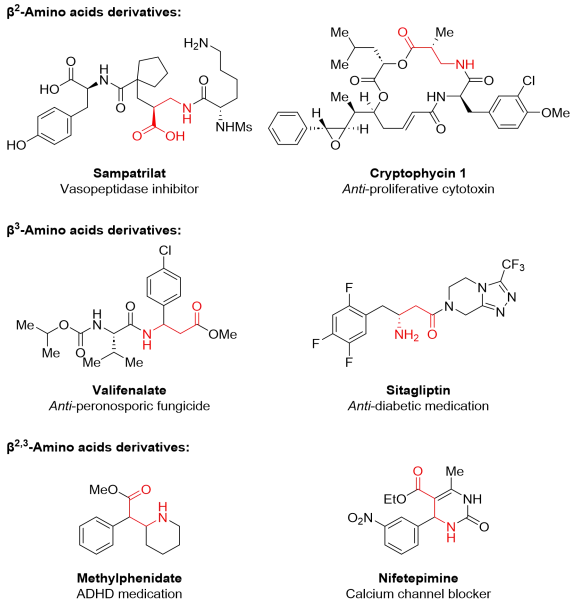

Figure 1. Bioactive species with β-amino acid skeletons.

The α-arylation of carbonyl compounds was first reported by Semmelhack group while synthesizing cephalotaxinone in the presence of $Ni(COD)_2$[3–4]. Following these works, reports by Miura group, Buchwald group, and Hartwig group described palladium-catalyzed intermolecular α-arylations independently[5–7]. In 2007, Hara group successfully achieved α-arylations and Buchwald–Hartwig aminations by employing a divalent nickel catalyst with an NHC ligand under more rigorous reaction conditions compared to palladium-catalyzed reactions[8]. An article by MacMillan group highlighted that the reductive eliminations of divalent palladium species are exothermic, while those of divalent nickel species are endothermic[9]. However, the reductive eliminations of trivalent nickel species are exothermic. By utilizing the electrochemical protocol, the conversion of divalent nickel species to trivalent at the anode can be regulated, facilitating the reductive elimination processes.

Electrochemical synthesis can be categorized into electrochemical oxidation, electrochemical reduction, and paired electrolysis. Electrochemical oxidation and electrochemical reduction involve using a single electrode as the working electrode, with the consumption of additional reagents or itself on another electrode to balance charges. In contrast, paired electrolysis allows both the anode and cathode to serve as working electrodes, maximizing energy utilization and atom economy, and enabling control over nickel's various oxidation states.

In our previous works, our group successfully formed C–O, C–N, C–C, and C–S bonds using the paired electrolysis strategy[10–14]. However, combining α-arylation with paired electrolysis is demanding due to the requirement for flawlessly matched generation rates of both anodic and cathodic reactive intermediates. Herein, we aimed to overcome those challenges by preparing α-aryl-α-cyanoacetates, which can be reduced to high-value-added α-aryl-β-amino acids, from commercially available α-cyanoacetates and aryl bromides under mild reaction conditions. Eventually, we proposed a catalytic mechanism based on a sequence of mechanistic studies and DFT calculations.

Experimental Section

Reagents

All the commercial reagents used in this study were purchased from TCI, Adamas-beta, J&K, Macklin, Leyan, and Bidepharm. They were used without further purification unless specified. Nickel foam (NF) electrodes, reticulated vitreous carbon (RVC, 100 ppi porosity) electrodes, graphite sheet electrodes, and fluorine-doped tin oxide (FTO) electrodes were purchased from e-commerce platforms. Platinum sheet electrodes were purchased from Gaoss Union.

Unless otherwise stated, all the experiments were carried out in over-dried hand-made electrochemical reactors within a nitrogen-filled glovebox. Mixtures were electrolyzed with Xiamen University proprietary type power supplies or HSPY-600 type power supplies.

Thin-layer chromatography (TLC) was conducted on Huanghai pre-coated glass plates purchased from Yantai Jiangyou Silica Gel Development Co., LTD. Spots of TLC plates were visualized using UV light (254 nm), iodine stain, potassium permanganate stain, or phosphomolybdic acid stain. Flash column chromatography was performed using Huanghai silica gel (200–300 or 300–400 mesh).

Electrochemical Reactor

Equipped with a stirring bar, a 10 mL heavy-walled test tube with a ground glass inner joint from Synthware served as the electrolytic cell. An electrode holder from Gaoss Union was used, which consisted of a gold-plated copper rod, an insulated polytetrafluoroethylene protector, and a platinum sheet. The anode, a 0.5 × 1.0 × 0.2 cm RVC cube, was held in place by the electrode holder. The cathode, a thin NF piece measuring 2.0 × 3.0 cm, was suspended by a copper wire. The electrode holder and the copper wire were fixed in a rubber stopper through two pre-drilled holes. Then, the rubber stopper was inserted into the joint of the test tube (**Figure 2**).

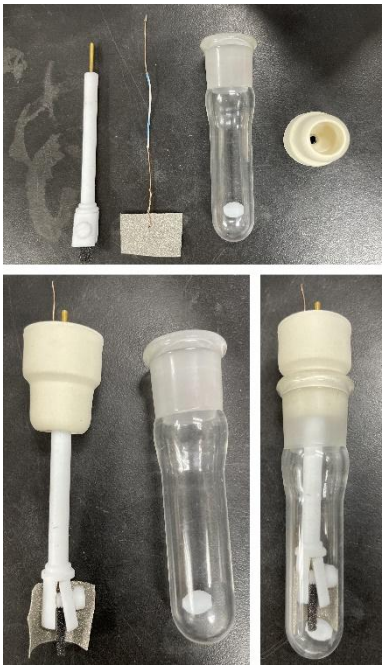

Figure 2. Electrochemical reactor.

Characterizations

^{1}H NMR, ^{11}B NMR, ^{13}C NMR, ^{19}F NMR, and ^{31}Si NMR spectra were recorded on an Agilent 400-MR DD2, a Varian 400-MR, or a Bruker Avance III HD (400 MHz, 128 MHz, 101 MHz, 377 MHz, and 79 MHz respectively) at State Key Laboratory of Organometallic Chemistry, SIOC, CAS. The chemical shifts for ^{1}H NMR and ^{31}Si NMR were reported relative to the tetramethylsilane (δ 0.00 ppm, 1% v/v solution in deuterated chloroform). The chemical shifts for ^{13}C NMR were reported relative to deuterated chloroform (δ 77.16 ppm). Multiplicities were reported according to the following abbreviations: s = singlet, d = doublet, t = triplet, q = quartet, h = heptlet, m = multiplet, and br = broad.

High-resolution mass spectra (HRMS) were recorded on a Thermo Fisher Scientific LTQ FTICR-MS, a JEOL-AccuTOF-GCv4G-GCT MS, or an Agilent Technologies 7250 GCQTOF in DART+, FI+, or EI+ mode at State Key Laboratory of Organometallic Chemistry, SIOC, CAS or Center of Mass Spectrometry, SIOC, CAS.

Infrared spectra were recorded on a Bruker tensor 27 at State Key Laboratory of Organometallic Chemistry, SIOC, CAS.

Elemental analyses were carried out on an Elementar vario MicroCube at Laboratory of Elemental Analysis, SIOC, CAS.

Electroanalyses

Alumina powders, polishing pads, platinum counter electrodes, glassy carbon working electrodes, and silver wire reference electrodes were purchased from Gaoss Union. Cyclic voltammograms (CV) were recorded on a CHI760E workstation at room temperature within a nitrogen-filled glovebox. The reference electrode consisted of a silver wire electrode and 0.1 mol/L of $AgNO_3$ solution in acetonitrile, calibrated by 5 mmol/L Fc^{+}/Fc before CV tests (**Figure 3**).

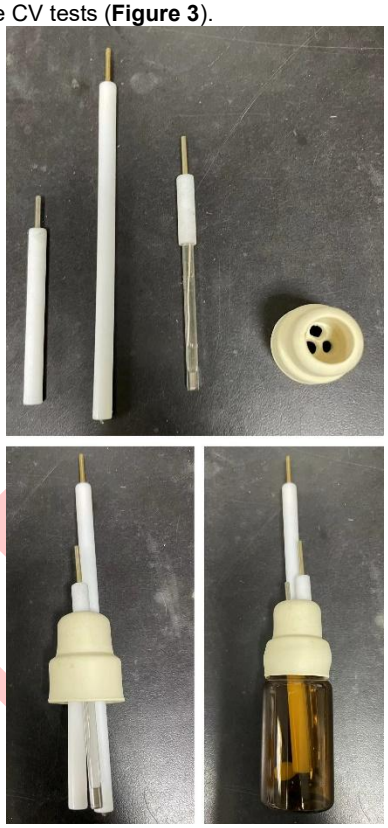

Figure 3. Three-electrode system.

Test data were plotted using OriginPro learning edition. Anodic peak potentials (E_{pa}) and cathodic peak potentials (E_{pc}) of each peak were labeled on the plots. For reversible and quasi-reversible redox couples, half-wave potentials ($E_{1/2}$), averages between E_{pa} and E_{pc}, were used to estimate the reduction potentials (E_{red}). For irreversible redox couples, inflection-point potentials (E_i), potentials where $\partial^2 i/\partial E^2 = 0$ at $\partial i/\partial E \neq 0$, were employed to estimate E_{red}[15].

Calculational Studies

All the calculational works were performed with Gaussian 16 A.03 packages[16] on the high-performance computing cluster of State Key Laboratory of Organometallic Chemistry, SIOC, CAS. DFT calculations were carried out using PBE0 functional[17] including D3 version of Grimme's empirical dispersion correction[18] with Becke–Johnson damping[19]. Optimizations and single-point calculations were conducted in DMAc (SMD model[20]) with def2-SVP basis sets[21–22] and def2-TZVP basis sets[21–22], respectively. Frequency analyses were carried out to ensure that substances, products, and intermediates (IM) had no imaginary frequency while each transition state (TS) only possessed one. Intrinsic reaction coordinate (IRC) analyses were carried out to confirm the reaction paths connecting their reactant, transition state, and product. The calculation results were represented by the Gibbs free energy change ΔG in kcal/mol. The solvated Gibbs free energy was obtained by combining the electronic energy calculated at PBE0-

D3(BJ)/def2-TZVP-SMD(DMAc) with the thermal-corrected energy calculated at PBE0-D3(BJ)/def2-SVP-SMD(DMAc). 3D representations were generated by CYLview software[23]. Potential energy diagrams were generated by ChemDraw Energy Diagram Plotter tool[24]. The analysis of weak interaction was carried out using Multiwfn software[25] with an independent gradient model based on Hirshfeld partition of molecular density (IGMH)[26], and the result was visualized using VMD software[27][28].

Preparations

*Preparation of Phenyl α-Cyanoacetate (**1h**)*

A mixture of α-cyanoacetate acid (0.85 g, 10 mmol, 1.0 equiv), phenol (1.04 g, 11 mmol, 1.1 equiv), *N*,*N*′-dicyclohexylcarbodiimide (DCC, 2.27 g, 11 mmol, 1.1 equiv), and 4-(dimethylamino)pyridine (DMAP, 0.12 g, 1 mmol, 0.1 equiv) in anhydrous DCM (15 mL) was stirred for 12 hours at room temperature on a fume hood. Then, the mixture underwent filtration with celite followed by concentration in vacuo. The crude residue was purified by flash column chromatography on silica gel (PE/EA = 6:1–2:1, R_f(PE/EA=6:1) = 0.26), affording phenyl α-cyanoacetate **1h** as a brown oil (562.5 mg, 35% yield).

*Preparation of 2-(4-Bromophenyl)-4,4,5,5-tetraethyl-1,3,2-dioxaborolane (**2e**)*

It was synthesized according to the reference[29]: a mixture of 4-bromophenylboronic acid (1.00 g, 5 mmol, 1.0 equiv) and 3,4-diethyl-hexane-3,4-diol (872 mg, 5 mmol, 1.0 equiv) in anhydrous DCM (50 mL) was stirred overnight at room temperature on a fume hood. After being concentrated in vacuo, the mixture was diluted with EA. The organic phase was washed three times with saturated brine, dried over anhydrous Na_2SO_4, filtered, and concentrated in vacuo. Then, the crude residue was purified by flash column chromatography on silica gel (PE, R_f(PE) = 0.57), affording 2-(4-bromophenyl)-4,4,5,5-tetraethyl-1,3,2-dioxaborolane **2e** as a colorless and transparent oil (1.4726 g, 87% yield).

Preparations of α-Aryl-α-cyanoacetates

A suspension of $NiBr_2$·glyme (6.2 mg, 0.02 mmol, 10 mol%), 5,5′-dimethyl-2,2′-bipyridine (5,5′-Me_2-bpy, 5.5 mg, 0.03 mmol, 15 mol%), and tetrabutylammonium bromide (TBABr, 129 mg, 0.4 mmol, 2.0 equiv) in anhydrous DMAc (1.0 mL) was stirred for 15 minutes until its color changed from turquoise to light green. α-Cyanoacetate **1** (0.3 mmol, 1.5 equiv), aryl bromide **2** (0.2 mmol, 1.0 equiv), DMAc (1.0 mL), and 1,8-diazabicyclo[5.4.0]undec-7-ene (DBU, 61 μL, 0.4 mmol, 2.0 equiv) were added to the solution, and the solution color changed to yellowish brown. The hand-made electrochemical reactor was assembled, sealed with Parafilm, and transferred to a fume hood. The mixture was galvanostatically electrolyzed at 4.0 mA and 30 °C for 4 or 6 hours. The resulting solution was diluted with EA. The organic phase was washed three times with saturated aqueous NH_4Cl solution, dried over anhydrous Na_2SO_4, filtered, and concentrated in vacuo. The crude residue was purified by flash column chromatography on silica gel to afford the corresponding desired product.

Results and Discussion

Initially, we picked up commercially available *tert*-butyl cyanoacetate **1a** and 4-bromobenzotrifluoride **2a** as model substrates. In the presence of 10 mol% of $NiBr_2$·glyme, 15 mol% of 4,4′-OMe_2-bpy, 2.0 equiv of TBABr, and 2.0 equiv of LiHMDS in DMAc at room temperature, the target product *tert*-butyl 2-cyano-2-(4-(trifluoromethyl)phenyl)acetate **3aa** was obtained in 23% proton NMR yield after galvanostatic electrolysis at 4.0 mA for 6 hours (**Table 1**, Entry 1). Only trace **3aa** was detected when omitting a current, $NiBr_2$·glyme, or a base, indicating that an oscillation of oxidation states of nickel species and a deprotonation step played crucial roles in the catalytic cycle (**Table 1**, Entries 2–4). DMAc-insoluble bases such as K_2CO_3 and ^{t}BuOK did not induce this transformation (**Table 1**, Entries 5–6), while DBU gave **3aa** in 51% yield (**Table 1**, Entry 7). Using low-conductivity THF as the solvent, no **3aa** was observed (ε_r(DMAc) = 38.85, ε_r(DMF) = 38.25, ε_r(THF) = 7.52[30], **Table 1**, Entry 9). The ratio of **1a**/**2a** was increased to 1.5:1 because of the decomposition of **1a**, and the reaction time was decreased to 4 hours to avoid the side reaction of **3aa** after the complete consumption of **2a**, leading to the yield of **3aa** being raised to 71% (**Table 1**, Entry 12). When utilizing a zerovalent nickel as the catalyst precursor instead of a divalent nickel and stirring without any current, only 16% of 4,4′-bis(trifluoromethyl)-1,1′-biphenyl was produced (**Table 1**, Entry 13). Quick evaluations of ligands revealed that electron-rich bpy-type ligands (**Table 1**, Entries 12, 14–15) brought higher yields than electron-deficient bpy-type ligands (**Table 1**, Entry 17). Notably, the 6,6′-disubstituted bpy-type ligand caused a sharp decline in the yield due to the steric hindrance of 6- and 6′-positions (**Table 1**, Entry 16). Reactive species generated from electrode reactions have been decomposed or deactivated in lower temperatures before participating in the slow catalytic cycle. Apart from that, to ensure the reproducibility of this temperature-sensitive reaction during different seasons, a constant-temperature oil bath at 30 °C was taken, although higher energy consumption (**Table 1**, Entry 18). Aryl chloride **2a-Cl** (4-CF_3-C_6H_4-Cl), iodide **2a-I** (4-CF_3-C_6H_4-I), and triflate **2a-OTf** (4-CF_3-C_6H_4-OTf) could also achieve this conversion, albeit with lower yields than aryl bromide **2a** (**Table S4**). A decrease in the yield was observed when using a graphite sheet as the anode, which is another form of carbon electrode (**Table S9**). This could be attributed to its smaller specific surface area in comparison to the RVC electrode.

Table 1. Selected optimizations of reaction conditions (see Supporting Information for details).

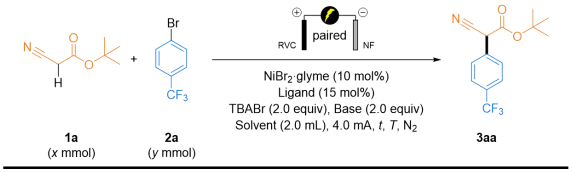

Entry	Base	Solvent	*x*	*y*	*t* (h)	Ligand	*T* (°C)	Yield[a]
1	LiHMDS	DMAc	0.2	0.2	6.0	4,4′-OMe_2-bpy	r.t.	23%
2[b]	LiHMDS	DMAc	0.2	0.2	6.0	4,4′-OMe_2-bpy	r.t.	2%
3[c]	LiHMDS	DMAc	0.2	0.2	6.0	4,4′-OMe_2-bpy	r.t.	2%
4	None	DMAc	0.2	0.2	6.0	4,4′-OMe_2-bpy	r.t.	1%
5	K_2CO_3	DMAc	0.2	0.2	6.0	4,4′-OMe_2-bpy	r.t.	n.d.
6	^tBuOK	DMAc	0.2	0.2	6.0	4,4′-OMe_2-bpy	r.t.	1%
7	DBU	DMAc	0.2	0.2	6.0	4,4′-OMe_2-bpy	r.t.	51%
8	DBU	DMF	0.2	0.2	6.0	4,4′-OMe_2-bpy	r.t.	22%
9	DBU	THF	0.2	0.2	6.0	4,4′-OMe_2-bpy	r.t.	n.d.
10	DBU	DMAc	0.2	0.4	6.0	4,4′-OMe_2-bpy	r.t.	41%
11	DBU	DMAc	0.3	0.2	6.0	4,4′-OMe_2-bpy	r.t.	59%
12	DBU	DMAc	0.3	0.2	4.0	4,4′-OMe_2-bpy	r.t.	71%[d]
13[b][e]	DBU	DMAc	0.3	0.2	4.0	4,4′-OMe_2-bpy	r.t.	n.d.
14	DBU	DMAc	0.3	0.2	4.0	5,5′-OMe_2-bpy	r.t.	62%
15	DBU	DMAc	0.3	0.2	4.0	5,5′-Me_2-bpy	r.t.	78%
16	DBU	DMAc	0.3	0.2	4.0	6,6′-Me_2-bpy	r.t.	4%
17	DBU	DMAc	0.3	0.2	4.0	5,5′-$(CF_3)_2$-bpy	r.t.	4%
18	DBU	DMAc	0.3	0.2	4.0	5,5′-Me_2-bpy	30	81% (71%)

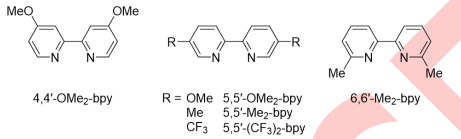

[a] Yields were determined by proton NMR using dibromomethane as an internal standard. The isolated yield is shown in parentheses. n.d. = Not detected. [b] Without a current. [c] Without $NiBr_2$·glyme. [d] No **2a** was detected after the electrolysis. [e] With 50 mol% of $Ni(COD)_2$ instead of 10 mol% of $NiBr_2$·glyme. With 75 mol% of 4,4′-OMe_2-bpy.

Subsequently, we investigated the scope of cyanoacetates under optimized reaction conditions (**Figure 4**). The corresponding desired products (**3aa**–**3ga**) of good isolation yields were obtained using alkyl cyanoacetates (**1a**–**1g**). Notably, it was observed that the conversion of benzyl cyanoacetate **1g** was not adversely affected by the presence of the reactive benzylic position. Phenyl cyanoacetate **1h** did not undergo this transformation, as evident from the crude proton NMR spectrum which showed that 0.9 equiv of **1h** remained out of the initial 1.5 equiv. It was suggested that the bulky phenyl group near the α-site might be responsible for its lack of reactivity. Additionally, allyl cyanoacetate **1i** was found to decompose under the given reaction conditions completely.

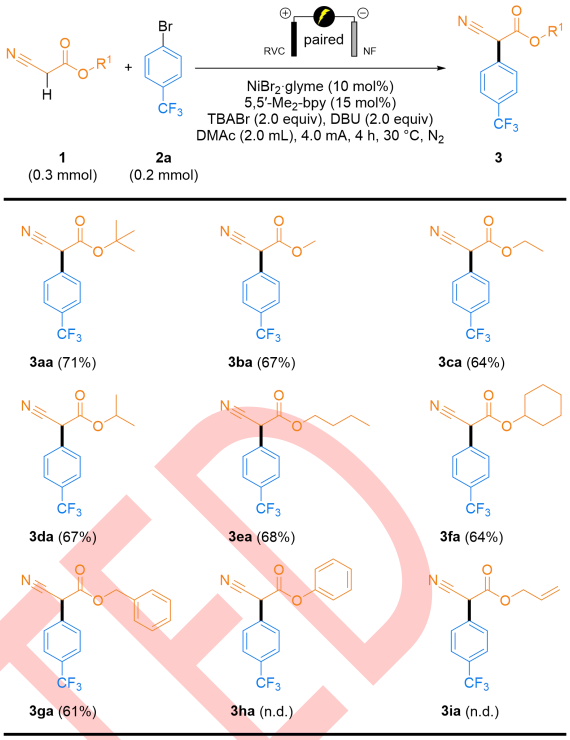

Figure 4. Evaluations of α-cyanoacetates.

Next, various aryl bromides were explored under the same conditions. Aryl bromides bearing electron-withdrawing groups afforded desired products in good to excellent yields (**Figure 5**). The tolerance of the alkyne group (**3af**) demonstrated a lower likelihood of forming a radical intermediate in the reaction process. The presence of a nitro group in **2k** resulted in a TLC plate displaying disordered plots. Steric hindrance resulted in the exclusive formation of dehalogenation products for both 1-bromonaphthalene **2l** and 4-bromo-1-naphthonitrile **2m**. Notably, the classic boronic ester, 2-(4-bromophenyl)-4,4,5,5-tetramethyl-1,3,2-dioxaborolane **2e′** (4-Br-C_6H_4-Bpin), afforded the corresponding product **3ae′** in 51% NMR yield. Still, the purification of **3ae′** was troublesome due to undesired over-absorption, strong tailing, and similar R_f values of **2e′** and **3ae′**. A novel boronic ester developed by Ikawa group[29], 2-(4-bromophenyl)-4,4,5,5-tetraethyl-1,3,2-dioxaborolane **2e** (4-Br-C_6H_4-B(Epin)), produced the corresponding product with a separation yield of 71% and no tailing. Our DFT calculations revealed that two of four ethyl groups in this boronic ester dynamically "blocked" the unoccupied orbitals of the boron atom (**Figure 6**, down. See **Figure S5** for the IGMH analysis).

When evaluating aryl bromides bearing electron-donating groups, it was observed that the proton NMR signals of α-H atoms in the resulting products were absent. Subsequent characterizations indicated that these products had dimeric structures (**Figure 7**). 1-Bromo-4-(methoxy)benzene **2n** and 2-bromo-5-(trifluoromethyl)pyridine **2o** also afforded self-coupling products **4an** and **4ao**. Notably, 4-bromo-1,1′-biphenyl **2j** yielded both a monomeric product **3aj** and a self-coupling product **4aj**. During the synthesis of **4an** on a large scale, a small amount of **3an** was separated from the mixture in a 3% yield. Such a low

yield was onerous to distinguish on the TLC plate during the 0.2 mmol-scale reaction. These observations suggested that the self-coupling product **4** might be generated from **3**.

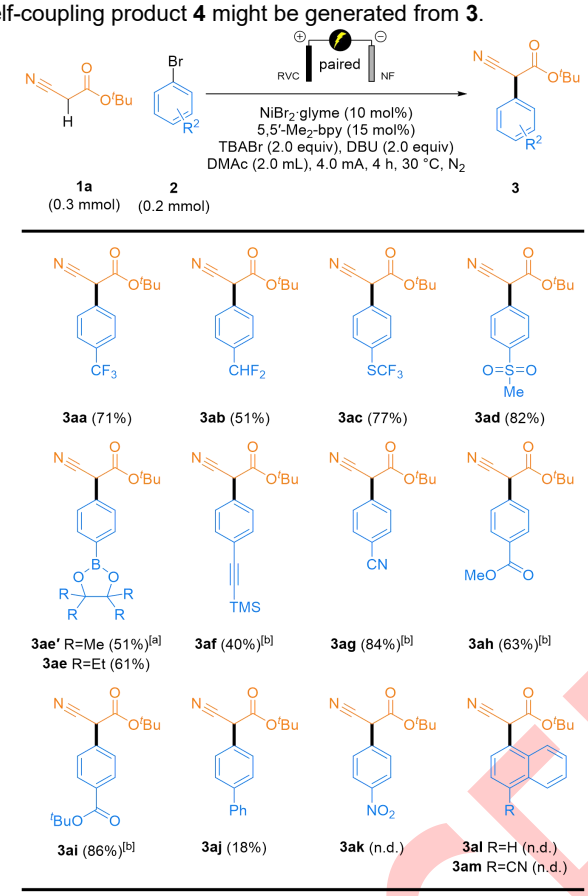

[a] Yields were determined by proton NMR using dibromomethane as an internal standard. [b] Electrolyzed for 6 hours.

Figure 5. Evaluations of aryl bromides bearing electron-withdrawing groups.

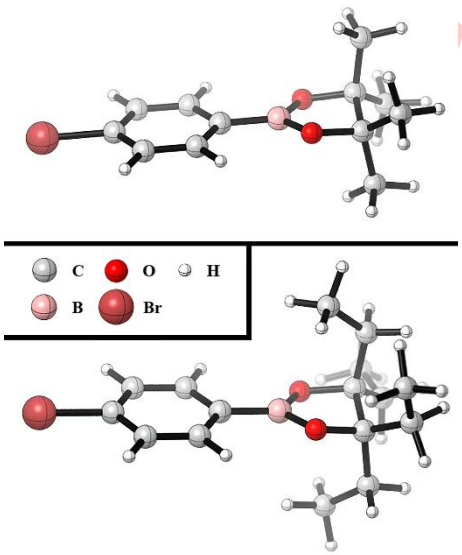

Figure 6. 3D structures of 4-Br-C_6H_4-Bpin **2e'** (up) and 4-Br-C_6H_4-B(Epin) **2e** (down).

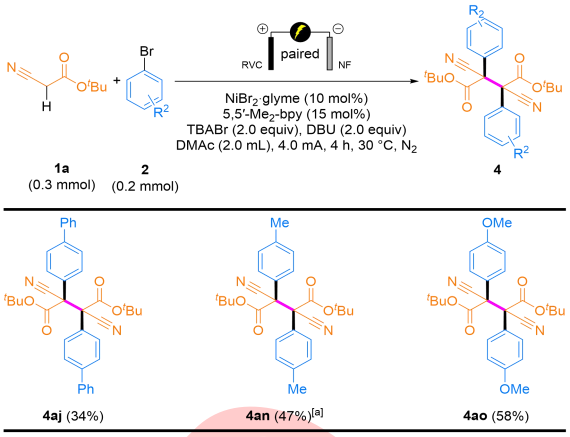

[a] Electrolyzed for 6 hours.

Figure 7. Evaluations of aryl bromides bearing electron-donating groups.

We devised a mechanism to clarify the formation of the self-coupling product **4** (**Scheme 1**). In the presence of base DBU, the acidic α-site proton of the desired product is rapidly absorbed, forming a reactive intermediate **3-anion**. **3-anion** bearing an electron-donating group exhibits a lower reduction potential. As a result, it is more prone to oxidize at the anode's superficial layer, generating a radical **3-radical**. Conversely, **3-anion** with an electron-withdrawing group is hardly oxidized to the radical, yielding the desired product after subsequent working-up steps.

The Gibbs free energies of **3-anion** and **3-radical** with various substituted groups were calculated at PBE0-D3(BJ)/def2-TZVP-SMD(DMAc)//PBE0-D3(BJ)/def2-SVP-SMD(DMAc). The differences between the Gibbs free energies of **3-anion** and **3-radical** were substituted into Nernst Equation to determine relative reduction potentials (**Table 2**, see Supporting Information for calculation protocols). The **3-anion** that forms the self-coupling product **4** has a lower reduction potential. In the case of **3aj-anion**, it has a moderate reduction potential, yielding both **3aj** and **4aj** simultaneously.

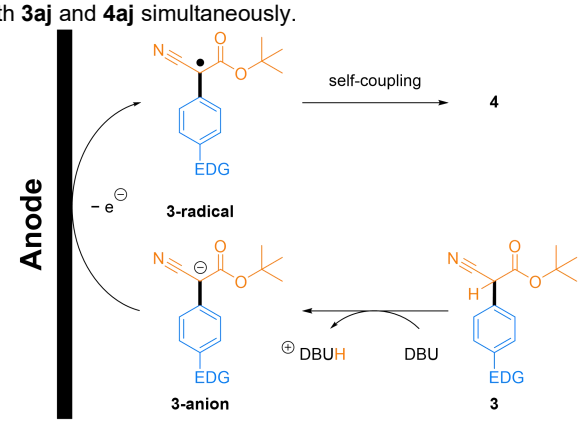

Scheme 1. Proposed formation mechanism of the self-coupling product **4**.

Table 2. DFT calculations of relative reduction potentials (vs SHE).

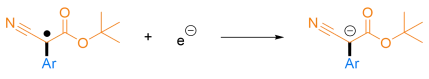

Entry	Ar	G(3-radical) (hartree)	G(3-anion) (hartree)	E_{red} (V)	Product Type
1	H	−477.456019	−477.623715	0.282	-
2	F_3C	−1045.151159	−1045.318921	0.284	**3**
3	F_3CS	−1443.212811	−1443.380928	0.294	**3**
4	(Epin)B	−1275.504322	−1275.667444	0.158	**3**
5	Ph	−939.076787	−939.23613	0.055	**3+4**
6	Me	−747.534187	−747.690877	−0.017	**4**
7	MeO	−822.695455	−822.847737	−0.137	**4**

Several cyclic voltammetry tests were performed within a nitrogen-filled glovebox. After conducting a preliminary trial (**Figure S3**), we judiciously chose a switching potential to prevent excessive reduction of the monovalent nickel species to the zerovalent state. The voltammogram depicted the quasi-reversibility of the $L_nNi^{II}Br_2/L_nNi^0$ redox couple with $E_{1/2}$ of −1.736 V (**Figure 8**, black line), which is a double-electron process according to the electroanalyses by Baran group[31]. Upon the addition of 1-bromo-4-(trifluoromethyl)benzene **2a**, the cathodic peak current of the $L_nNi^{II}Br_2/L_nNi^0$ couple escalated, while the anodic peak became less distinguishable (**Figure 8**, red line), even at a scan rate of 1000 mV/s (**Figure S4**). This suggested a rapid oxidative addition of L_nNi^IBr to **2a** (E_rC_i process), whose dimeric form, $[L_nNi^IBr]_2$, is unreactive[32]. Noteworthily, the oxidative addition from a zerovalent Ni species is less favorable than from a monovalent Ni species thermodynamically[33]. It was speculated that L_nNi^IBr was generated by the comproportionation of $L_nNi^{II}Br_2$ and L_nNi^0. The immediate reduction of the $L_nNi^{III}ArBr_2$ species coupled with the increase in the concentration gradient ∇c of $L_nNi^{II}Br_2$ led to the steep increase of the cathodic peak current. Furthermore, two new peaks (E_{pc} = −2.113 V, E_{pa} = −2.011 V) of a quasi-reversible response appeared (**Figure 8**, red line). The more negative $E_{1/2}$ value of −2.062 V could be identified as the $[Ni^{II}]/[Ni^I]$ couple rather than the $[Ni^{III}]/[Ni^{II}]$ couple. It was hypothesized that this response corresponded to the redox of the $L_nNi^{II}ArBr/L_nNi^IAr$ couple[34]. $L_nNi^{II}ArBr$ was formed through the reduction of the $L_nNi^{III}ArBr_2$ species.

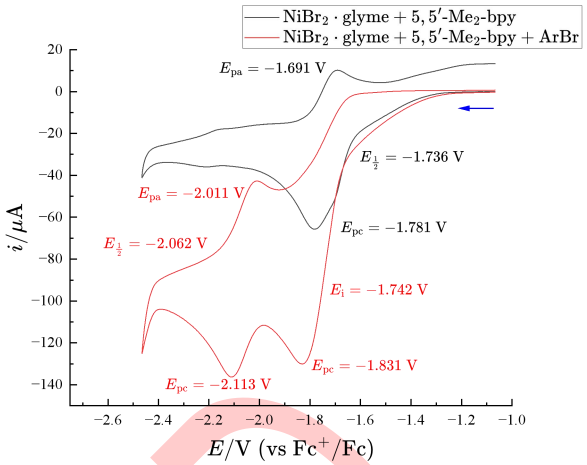

[a] Black line: $NiBr_2$·glyme (0.10 mmol), 5,5′-Me_2-bpy (0.15 mmol), $TBAPF_6$ (2.0 mmol), DMAc (10.0 mL). The scan rate was 100 mV/s. The solution resistance of 70.6 Ω was fully compensated. Red line: $NiBr_2$·glyme (0.10 mmol), 5,5′-Me_2-bpy (0.15 mmol), 4-CF_3-C_6H_4-Br (1.0 mmol), $TBAPF_6$ (2.0 mmol), DMAc (10.0 mL). The scan rate was 100 mV/s. The solution resistance of 72.3 Ω was fully compensated.

Figure 8. Cyclic voltammograms.

Based on the above observations, we proposed the following mechanism (**Scheme 2**). Initially, a catalytic amount of the $NiBr_2$ species is reduced at the cathode to form a zerovalent nickel species. The low-valent Ni^I species generated by the comproportionation readily undergoes an oxidative addition with the aryl bromide **2**, generating a trivalent nickel intermediate **INT1**. Then, **INT1** is reduced at the cathode to form a divalent nickel species **INT3**. **INT3** can undergo ligand exchange with an excess of **1-anion** in the solution, where one bromide ion is replaced, forming **INT4**. **INT4** migrates to the anode and undergoes an oxidation to form a trivalent nickel species **INT6**. Finally, the high-valent nickel species quickly undergoes a reductive elimination, releasing the product **3** spontaneously and returning to the monovalent state.

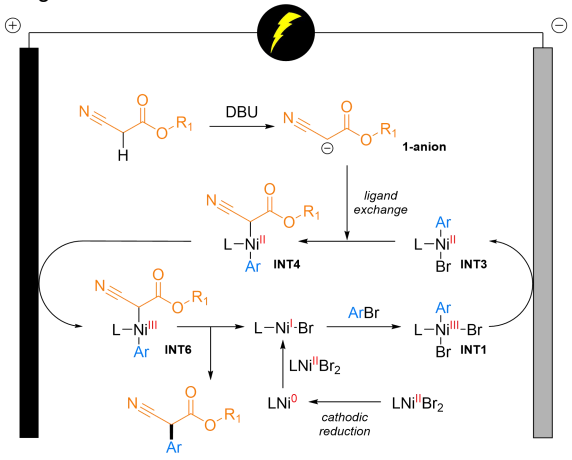

Scheme 2. Proposed mechanism.

At the same level of theory mentioned earlier, we performed DFT calculations for this process. The relative Gibbs free energies of each intermediate and transition state are shown in **Figure 9**. It is noticed that the conformation of **1a-anion** has some influence on the Gibbs free energies of each intermediate, but the overall trends are very close. Oxidative additions, ligand exchanges, and reductive eliminations have low-energy barriers ($\Delta G^{\neq}$ < 20 kcal/mol) that allow overcoming at room temperature. The energy barrier of the reductive elimination of the divalent nickel species **INT4** was calculated subsequently (**Figure 10**, left). The reductive elimination of **INT4** requires passing through a high-energy-barrier transition state **TS4** ($\Delta G^{\neq}$ > 20 kcal/mol) and is unspontaneous (ΔG > 0) at room temperature. For this reason, thermal chemical reactions catalyzed by the Ni^0/Ni^{II} pair often rely on strong heating[8]. In contrast, the reductive elimination of the trivalent nickel species **INT6** requires passing through a low-energy-barrier transition state **TS3** ($\Delta G^{\neq}$ < 20 kcal/mol) and is spontaneous (ΔG < 0) at room temperature (**Figure 10**, right). These also illustrate the advantage of adjusting the oxidation states of nickel species through an electrochemical protocol.

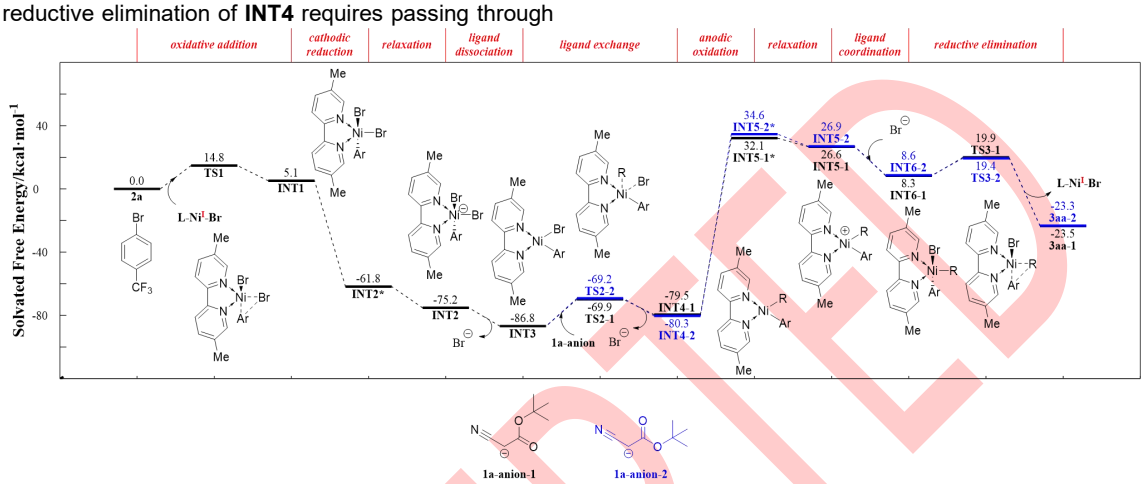

Figure 9. DFT calculations of the proposed mechanism at PBE0-D3(BJ)/def2-TZVP-SMD(DMAc)//PBE0-D3(BJ)/def2-SVP-SMD(DMAc).

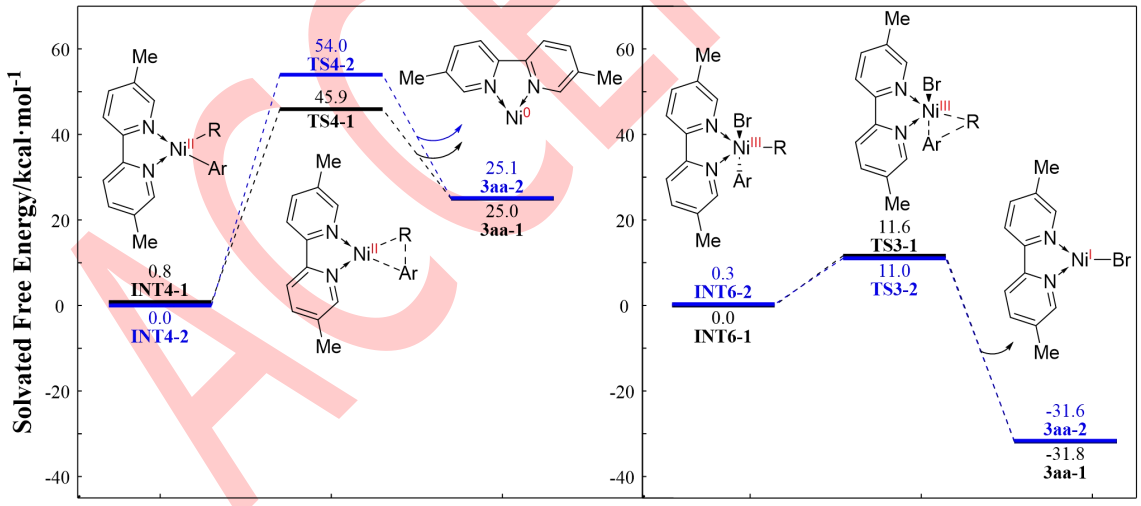

Figure 10. Energy barriers of reductive eliminations from divalent Ni species (left) and trivalent Ni species (right) at PBE0-D3(BJ)/def2-TZVP-SMD(DMAc)//PBE0-D3(BJ)/def2-SVP-SMD(DMAc).

Conclusion

Using the paired electrolysis protocol, we have successfully demonstrated a nickel-catalyzed α-arylation of α-cyanoacetates under mild conditions. Our electroanalyses and DFT calculational works supported our proposed enolate-intermediate-participated mechanism. In the meantime, DFT calculations showed that trivalent nickel species are more likely to undergo reduction eliminations compared to divalent ones. In light of these findings, we are conducting further investigations on α-arylations of broad-spectrum carbonyl compounds in our laboratory.

Supporting Information

The authors have cited additional references within the Supporting Information[35][36].

Acknowledgments

This work was financially supported by the National Key R&D Program of China (No. 2021YFA1500100), the NSF of China (Grants 21821002, 21772222, and 91956112), and the S&TCSM of Shanghai (Grants 20XD1425100 and 20JC1417100).

References

[1] Lelais G, Seebach D. β²-amino acids—syntheses, occurrence in natural products, and components of β-peptides[J]. Pept. Sci., 2004, 76(3): 206–243.

[2] Podlech J, Seebach D. The Arndt–Eistert Reaction in Peptide Chemistry: A Facile Access to Homopeptides[J]. Angew. Chem. Int. Ed., 1995, 34(4): 471–472.

[3] Semmelhack M F, Stauffer R D, Rogerson T D. Nucleophilic aromatic substitution via a new nickel-catalyzed process and via the $S_{RN}1$ reaction. Improved synthesis of cephalotaxinone[J]. Tetrahedron Lett., 1973, 14(45): 4519–4522.

[4] Semmelhack M F, Chong B P, Stauffer R D, Rogerson T D, Chong A, Jones L D. Total synthesis of the Cephalotaxus alkaloids. Problem in nucleophilic aromatic substitution[J]. J. Am. Chem. Soc., 1975, 97(9): 2507–2516.

[5] Satoh T, Kawamura Y, Miura M, Nomura M. Palladium-Catalyzed Regioselective Mono- and Diarylation Reactions of 2-Phenylphenols and Naphthols with Aryl Halides[J]. Angew. Chem. Int. Ed. Engl., 1997, 36(16): 1740–1742.

[6] Palucki M, Buchwald S L. Palladium-Catalyzed α-Arylation of Ketones[J]. J. Am. Chem. Soc., 1997, 119(45): 11108–11109.

[7] Hamann B C, Hartwig J F. Palladium-Catalyzed Direct α-Arylation of Ketones. Rate Acceleration by Sterically Hindered Chelating Ligands and Reductive Elimination from a Transition Metal Enolate Complex[J]. J. Am. Chem. Soc., 1997, 119(50): 12382–12383.

[8] Matsubara K, Ueno K, Koga Y, Hara K. Nickel−NHC-Catalyzed α-Arylation of Acyclic Ketones and Amination of Haloarenes and Unexpected Preferential *N*-Arylation of 4-Aminopropiophenone[J]. J. Org. Chem., 2007, 72(14): 5069–5076.

[9] Terrett J A, Cuthbertson J D, Shurtleff V W, MacMillan D W C. Switching on elusive organometallic mechanisms with photoredox catalysis[J]. Nature, 2015, 524: 330–334.

[10] Liu D, Ma H-X, Fang P, Mei T-S. Nickel-Catalyzed Thiolation of Aryl Halides and Heteroaryl Halides through Electrochemistry[J]. Angew. Chem. Int. Ed., 2019, 58(15): 5033–5037.

[11] Liu D, Liu Z-R, Ma C, Jiao K-J, Sun B, Wei L, Lefranc J, Herbert S, Mei T-S. Nickel-Catalyzed *N*-Arylation of *NH*-Sulfoximines with Aryl Halides via Paired Electrolysis[J]. Angew. Chem. Int. Ed., 2021, 60(17): 9444–9449.

[12] Wei L, Wang Z-H, Jiao K-J, Liu D, Ma C, Fang P, Mei T-S. Esterification of Carboxylic Acids with Aryl Halides via the Merger of Paired Electrolysis and Nickel Catalysis[J]. J. Org. Chem., 2021, 86(22): 15906–15913.

[13] Wang Z-H, Wei L, Jiao K-J, Ma C, Mei T-S. Nickel-Catalyzed Decarboxylative Cross-Coupling of Indole-3-acetic Acids with Aryl Bromides by Convergent Paired Electrolysis[J]. Chem. Commun., 2022, 58(59): 8202–8205.

[14] Liu D, Liu Z-R, Wang Z-H, Ma C, Herbert S, Schirok H, Mei T-S. Paired electrolysis-enabled nickel-catalyzed enantioselective reductive cross-coupling between α-chloroesters and aryl bromides[J]. Nat. Commun., 2022, 13: 7318.

[15] Espinoza E M, Clark J A, Soliman J, Derr J B, Morales M, Vullev V I. Practical Aspects of Cyclic Voltammetry: How to Estimate Reduction Potentials When Irreversibility Prevails[J]. J. Electrochem. Soc., 2019, 166(5): H3175–H3187.

[16] Frisch M J, Trucks G W, Schlegel H B, Scuseria G E, Robb M A, Cheeseman J R, Scalmani G, Barone V, Petersson G A, Nakatsuji H, Li X, Caricato M, Marenich A V, Bloino J, Janesko B G, Gomperts R, Mennucci B, Hratchian H P, Ortiz J V, Izmaylov A F, Sonnenberg J L, Williams, Ding F, Lipparini F, Egidi F, Goings J, Peng B, Petrone A, Henderson T, Ranasinghe D, Zakrzewski V G, Gao J, Rega N, Zheng G, Liang W, Hada M, Ehara M, Toyota K, Fukuda R, Hasegawa J, Ishida M, Nakajima T, Honda Y, Kitao O, Nakai H, Vreven T, Throssell K, Montgomery Jr. J A, Peralta J E, Ogliaro F, Bearpark M J, Heyd J J, Brothers E N, Kudin K N, Staroverov V N, Keith T A, Kobayashi R, Normand J, Raghavachari K, Rendell A P, Burant J C, Iyengar S S, Tomasi J, Cossi M, Millam J M, Klene M, Adamo C, Cammi R, Ochterski J W, Martin R L, Morokuma K, Farkas O, Foresman J B, Fox D J. Gaussian 16[CP]. Wallingford, CT: Gaussian, Inc., 2016.

[17] Adamo C, Barone V. Toward reliable density functional methods without adjustable parameters: The PBE0 model[J]. J. Chem. Phys., 1999, 110: 6158–6170.

[18] Grimme S, Antony J, Ehrlich S, Krieg H. A consistent and accurate ab initio parametrization of density functional dispersion correction (DFT-D) for the 94 elements H-Pu[J]. J. Chem. Phys., 2010, 132: 154104.

[19] Grimme S, Ehrlich S, Goerigk L. Effect of the damping function in dispersion corrected density functional theory[J]. J. Comput. Chem., 2011, 32(7): 1456–1465.

[20] Marenich A V, Cramer C J, Truhlar D G. Universal Solvation Model Based on Solute Electron Density and on a Continuum Model of the Solvent Defined by the Bulk Dielectric Constant and Atomic Surface Tensions[J]. J. Phys. Chem. B, 2009, 113(18): 6378–6396.

[21] Weigenda F, Ahlrichsb R. Balanced basis sets of split valence, triple zeta valence and quadruple zeta valence quality for H to Rn: Design and assessment of accuracy[J]. Phys. Chem. Chem. Phys., 2005, 7(18): 3297–3305.

[22] Weigenda F. Accurate Coulomb-fitting basis sets for H to Rn[J]. Phys. Chem. Chem. Phys., 2006, 8(9): 1057–1065.

[23] Legault C Y. CYLView[CP]. 1.0b, Sherbrooke, QC: Université de Sherbrooke, 2009. http://www.cylview.org.

[24] Li Y-H. Energy Diagram Plotter CDXML[CP]. 3.5.2. Zenodo, 2023. https://doi.org/10.5281/zenodo.7634466.

[25] Lu T, Chen F. Multiwfn: A multifunctional wavefunction analyzer[J]. J. Comput. Chem., 2012, 33(5): 580–592.

[26] Lu T, Chen Q. Independent gradient model based on Hirshfeld partition: A new method for visual study of interactions in chemical systems[J]. J. Comput. Chem., 2022, 43(8): 539–555.

[27] Humphrey W, Dalke A, Schulten K. VMD: Visual molecular dynamics[J]. J. Molec. Graphics, 1996, 14(1): 33–38.

[28] Stone J E. An efficient library for parallel ray tracing and animation[D]. Rolla, MO: University of Missouri-Rolla, 1998. Link: https://scholarsmine.mst.edu/masters_theses/1747.

[29] Oka N, Yamada T, Sajiki H, Akai S, Ikawa T. Aryl Boronic Esters Are Stable on Silica Gel and Reactive under Suzuki–Miyaura Coupling Conditions[J]. Org. Lett., 2022, 24(19): 3510–3514.

[30] Haynes W M, Lide D R, Bruno T J. CRC Handbook of Chemistry and Physics[M]. 97th ed. Boca Raton, USA: CRC Press, 2016: 6-199–6-220.

[31] Kawamata Y, Vantourout J C, Hickey D P, Bai P, Chen L, Hou Q, Qiao W, Barman K, Edwards M A, Garrido-Castro A F, deGruyter J N, Nakamura H, Knouse K, Qin C, Clay K J, Bao D, Li C, Starr J T, Garcia-Irizarry C, Sach N, White H S, Neurock M, Minteer S D, Baran P S. Electrochemically Driven, Ni-Catalyzed Aryl Amination: Scope, Mechanism, and Applications[J]. J. Am. Chem. Soc., 2019, 141(15): 6392–6402.

[32] Till N A, Oh S, MacMillan D W C, Bird M J. The Application of Pulse Radiolysis to the Study of Ni(I) Intermediates in Ni-Catalyzed Cross-Coupling Reactions[J]. J. Am. Chem. Soc., 2021, 143(25): 9332–9337.

[33] Gutierrez O, Tellis J C, Primer D N, Molander G A, Kozlowski M C. Nickel-catalyzed cross-coupling of photoredox-generated radicals: uncovering a general manifold for stereoconvergence in nickel-catalyzed cross-couplings[J]. J. Am. Chem. Soc., 2015, 137(15): 4896–4899.

[34] Yakhvarov D G, Samieva E G, Tazeev D I, Budnikovaa Y G. The reactivity of 2,2′-bipyridine complexes in the electrochemical reduction of organohalides[J]. Russ. Chem. Bull., Int. Ed., 2002, 51: 796–804.

[35] Wrackmeyer B. Carbon-13 NMR spectroscopy of boron compounds[J]. Prog. NMR Spectrosc., 1979, 12(4): 227–259.

[36] Isse A A, Gennaro A. Absolute Potential of the Standard Hydrogen Electrode and the Problem of Interconversion of Potentials in Different Solvents[J]. J. Phys. Chem. B, 2010, 114(23): 7894–7899.

Entry for the Table of Contents

((Insert graphic for Table of Contents here (300 DPI resolution: up to 1240x1180 pixels with a maximum width 10.5 cm and height 10 cm).))

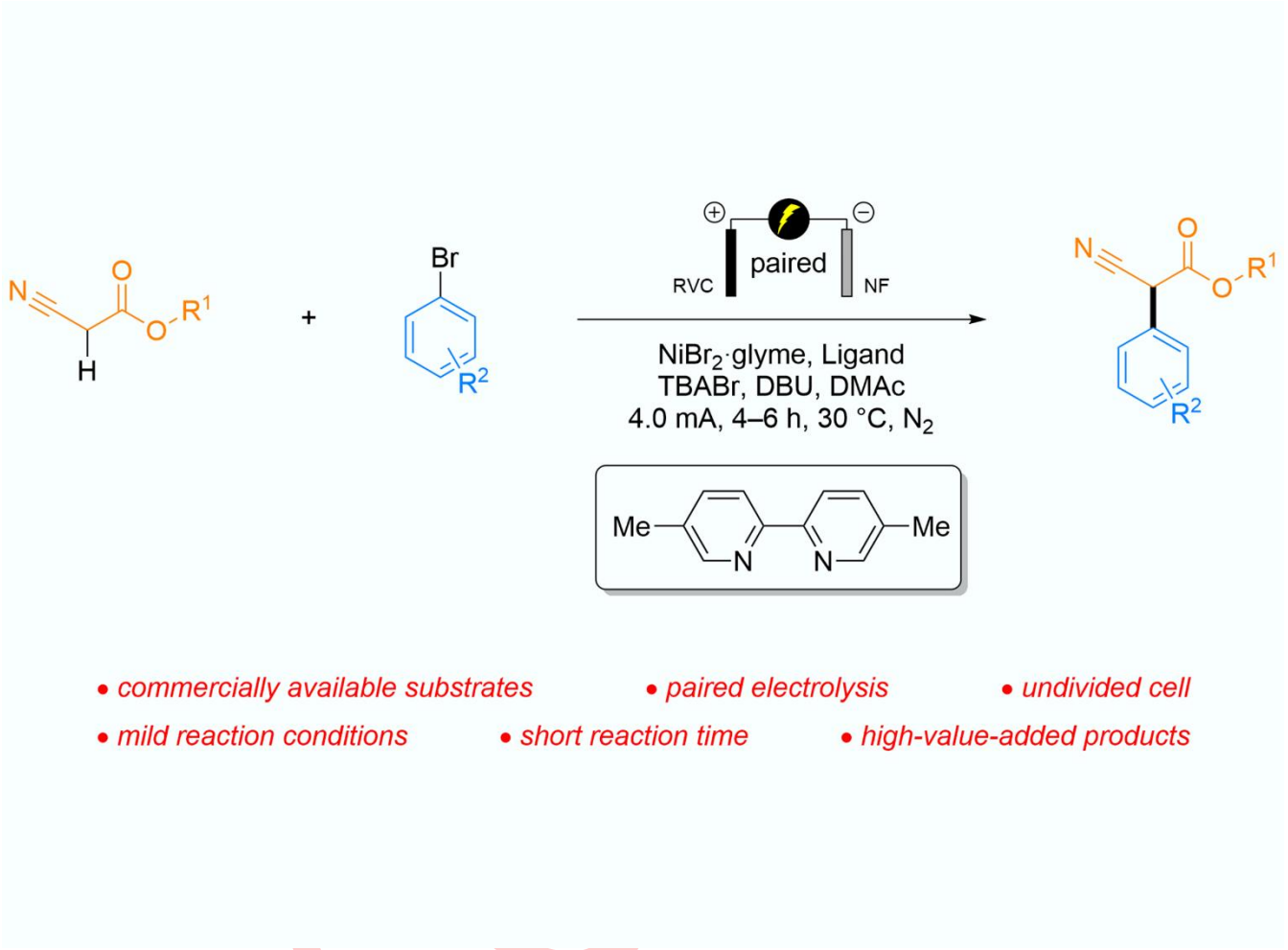

电化学促进的镍催化的α-氰基乙酸酯的α-芳基化反应

李子萌[a]，李章健[a,b]，Anat Milo[c]，方萍[a*]，梅天胜[a*]

（a. 中国科学院上海有机化学研究所金属有机国家重点实验室，中国科学院大学，上海 200032；b. 四川师范大学化学与材料科学学院，成都 610068；c. 本·古里安大学化学部，贝尔谢巴 841051）

摘要：β-氨基酸在医药领域有着广泛的应用。本文利用镍催化的成对电解策略，发展了一种羰基α-芳基化反应，实现了α-芳基-α-氰基乙酸酯的合成。产物可通过简单还原制备α-芳基-β-氨基酸，具有极高的附加价值。在温和条件下，以缺电子芳基溴与α-氰基乙酸酯为底物，可以良好的收率获得目标产物，且具有较好的官能团兼容性。当芳基溴过于富电子时，目标产物发生自偶联。使用 DFT 计算了产物负离子的还原电势，表明了富电子芳基取代使产物还原电势降低，更易于在阳极发生氧化。通过电化学分析和机理实验，推测为烯醇负离子配体交换型机理而非自由基加成型机理。

关键词：有机电合成；镍催化；成对电解；α-芳基化；DFT 计算